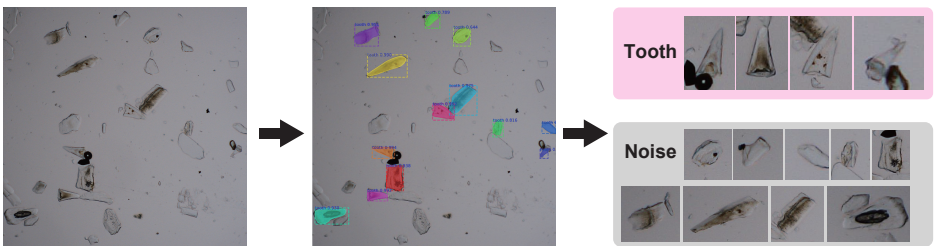
microscopic image
(1) detection by
Mask R-CNN
(2) classification by
EfficientNet-V2
Tooth
Noise

Automated detection of microfossil fish teeth from slide images using combined deep learning models

Kazuhide Mimura[a,b], Shugo Minabe[c], Kentaro Nakamura[b,c,a*], Kazutaka Yasukawa[b,c], Junichiro Ohta[b,c,a], Yasuhiro Kato[c,a,d]

[a]Ocean Resources Research Center for Next Generation, Chiba Institute of Technology, 2-17-1 Tsudanuma, Narashino, Chiba 275-0016, Japan.

[b]Frontier Research Center for Energy and Resources, School of Engineering, University of Tokyo, 7-3-1 Hongo, Bunkyo-ku, Tokyo 113-8656, Japan.

[c]Department of Systems Innovation, School of Engineering, The University of Tokyo, 7-3-1 Hongo, Bunkyo-ku, Tokyo 113-8656, Japan.

[d]Submarine Resources Research Center, Research Institute for Marine Resources Utilization, Japan Agency for Marine-Earth Science and Technology (JAMSTEC), 2-15 Natsushima-cho, Yokosuka, Kanagawa 237-0061, Japan.

Corresponding author:

Kentaro Nakamura

Department of Systems Innovation, School of Engineering, University of Tokyo,

7-3-1 Hongo, Bunkyo-ku, Tokyo 113-8656, Japan

Telephone: +81-3-5841-7089

E-mail: kentaron@sys.t.u-tokyo.ac.jp

Author contribution statement

Conceptualization, KM, SM, and KN; program coding, KM, SM; preparation of the dataset, KM and SM; investigation, KM and JO; writing—original draft preparation, KM KN and KY; writing—review and editing, all authors; supervision, KN, and YK; funding acquisition, KM, KN, KY, and YK. All the authors have read and agreed to the published version of the manuscript.

ABSTRACT

Microfossil fish teeth, known as ichthyoliths, provide a key constraint on the depositional age and environment of deep-sea sediments, especially pelagic clays where siliceous and calcareous microfossils are rarely observed. However, traditional methods for the observation of ichthyoliths require considerable time and manual labor, which can hinder their wider application. In this study, we constructed a system to automatically detect ichthyoliths in microscopic images by combining two open source deep learning models. First, the regions for ichthyoliths within the microscopic images are predicted by the instance segmentation model Mask R-CNN. All the detected regions are then re-classified using the image classification model

EfficientNet-V2 to determine the classes more accurately. Compared with only using the Mask R-CNN model, the combined system offers significantly higher performance (89.0% precision, 78.6% recall, and an F1 score of 83.5%), demonstrating the utility of the system. Our system can also predict the lengths of the teeth that have been detected, with more than 90% of the predicted lengths being within ± 20% of measured length. This system provides a novel, automated, and reliable approach for the detection and length measurement of ichthyoliths from microscope images that can be applied in a range of paleoceanographic and paleoecological contexts.

Keywords:

Deep learning;

Object detection;

Image classification;

Microfossils;

Ichthyolith

1. Introduction

Pelagic clay is a type of deep-sea sediment that covers more than one-third of the global ocean floor (Dutkiewicz

et al., 2015) and has long been regarded as an important medium for recording changes in atmospheric and oceanic circulation, surface ocean productivity, and the influx of extraterrestrial material in the pelagic realm (Kyte et al., 1993; Kyte, 1998; Kyte and Bostwick, 1995; Nozaki et al., 2019; Tanaka et al., 2022; Zhou and Kyte, 1992). The chemical composition of pelagic clay varies considerably despite its homogenous appearance, reflecting the fractions of its components, such as terrigenous dust, volcanic materials, hydrogenous and hydrothermal Fe-Mn oxides, and biogenic components (Dunlea et al., 2015a, 2015b; Leinen, 1987; Ren et al., 2021; Tanaka et al., 2022; Yasukawa et al., 2016, 2019; Ziegler et al., 2007).

Pelagic clay has recently received attention as a novel type of mineral resource for rare-earth elements and yttrium (REY), which are industrially critical metals, especially for technologies and products aiming toward carbon-neutrality. Pelagic clays enriched in REY, termed as “REY-rich mud” (Kato et al., 2011), were originally discovered in the deep-sea basin of the central North and eastern South Pacific Ocean. To date, they have been reported from the global ocean, including the western North Pacific (Bi et al., 2021; Fujinaga et al., 2016; Tanaka et al., 2020a, 2020b), central and South Pacific (Ohta et al., 2021; Sa et al., 2018; Zhou et al., 2020, 2021), Indian (Yasukawa et al., 2014, 2015; Yu et al., 2021; Zhang et al., 2017) and Atlantic Oceans (Menendez et al., 2017; Nakamura et al., 2015). Notably, the existence of “extremely REY-rich mud” in the western North Pacific Ocean (Iijima et al., 2016; Mimura et al., 2019; Takaya et al., 2018), together with the investigations of physical beneficiation techniques (Takaya et al., 2018) and by-product metal extraction (Yasukawa et al., 2018, 2020), further highlights the significance of pelagic clay as a promising mineral resource. Interestingly, the

74 accumulation of REY in pelagic clay was caused by changes in bioproductivity and ocean circulation, which
75 reflects changes in the Earth's climate system (Ohta et al., 2020). This indicates that examining environmental
76 changes recorded in pelagic clay is essential for understanding the genesis and distribution of industrially critical
77 metal resources, emphasizing the increasing importance of analyzing pelagic clay.

78 Depositional age is key information for understanding depositional environments of the seafloor sediment
79 because the environment has been affected by a secular change in global climate (Westerhold et al., 2020;
80 Zachos et al., 2008) and plate motion over geologic timescales (Müller et al., 2018). However, calcareous or
81 siliceous microfossils, which have commonly been used for constraining depositional ages of the seafloor
82 sediment, are not found in pelagic clay, owing to the dissolution of the fossils by undersaturation of carbonates
83 and silica in the deep-sea environment. This has hampered examination of the depositional environment and
84 exploration of the origin that controls distribution of deep-sea resources.

85 In contrast, fish teeth and denticles, known as ichthyoliths, are well preserved in almost all kinds of seafloor
86 sediments because they are composed of calcium phosphate, which is not easily dissolved (Sibert et al., 2014).
87 Therefore, ichthyoliths have been used as a key for constraining the depositional age of pelagic clay (Doyle et al.,
88 1974; Doyle and Riedel, 1979, 1985; Ohta et al., 2020). In addition, ichthyoliths are regarded as indicators of
89 depositional environments recently. The productivity of pelagic fish has been measured based on the
90 accumulation rate of ichthyoliths (Sibert et al., 2014, 2016, 2020; Sibert and Rubin, 2021), the evolution of
91 pelagic ecosystems has been explored based on variations in morphotypes (Sibert et al., 2018; Sibert and Rubin,

92 2021), and the distribution of pelagic fish has been studied based on variation in the length of fish teeth (Britten
93 and Sibert, 2020). Hence, establishing an effective method for ichthyolith observation will enable understanding
94 of the records on the evolution of pelagic realms which has long been a black box in Earth science.
95 Traditionally, ichthyolith analysis first involves extracting coarse-grained particles from the target sediment. By
96 observing these grains under a stereomicroscope, ichthyoliths are manually picked up and moved on to a slide
97 using a fine-pointed brush. This process, called 'handpicking', remains a common technique for both
98 stratigraphic and environmental research (Ohta et al., 2020; Sibert et al., 2017) and is one of the most
99 time-consuming processes in ichthyolith analysis. Slides with the ichthyoliths are then observed under a
100 microscope for detailed description and identification. Observers describe a range of features including their
101 outer shape, inner structures, and size (Britten and Sibert, 2020; Doyle and Riedel, 1979; Sibert et al., 2018),
102 which also requires considerable time and effort by experienced experts.
103 In comparison to these manual techniques, recent developments in computer vision have achieved promising
104 results in various fields including medicine, neuroscience, and robotics (Jo et al., 2017; Kim et al., 2018; Sakai et
105 al., 2018; Shoji et al., 2018; Suleymanova et al., 2018). Techniques in computer vision have also been applied in
106 the field of microfossil research for the tasks of classification and detection. The classification of microfossils
107 was first attempted by obtaining key morphological parameters from microfossil images (Marmo et al., 2006; Yu
108 et al., 1996), with support vector machines (SVMs) contributing to their classification according to the acquired
109 values (Apostol et al., 2016; Bi et al., 2015; Hu and Davis, 2005; Solano et al., 2018; Xu et al., 2020). Owing to

110 the development of convolutional neural networks (CNNs), deep learning based classification models have
111 successfully been used to determine the taxa of various microfossils including foraminifera and radiolarians
112 (Carvalho et al., 2020; Hsiang et al., 2019; Itaki et al., 2020; Keçeli et al., 2017; Marchant et al., 2020; Mitra et
113 al., 2019; Pires de Lima et al., 2020; Xu et al., 2020; Tetard et al., 2020). Although some of these classification
114 models achieve an accuracy of > 85% (Hsiang et al., 2019; Itaki et al., 2020; Marchant et al., 2020; Tetard et al.,
115 2020), large training datasets are often required, which creates the challenge of generating a large number of
116 images for each microfossil species. To address this problem, previous studies (Beaufort and Dollfus, 2004;
117 Hsiang et al., 2018; Itaki et al., 2020; Tetard et al., 2020) have proposed a method that captures the entire area of
118 a slide. In these studies, individual particles were extracted from the image based on thresholding, which may
119 reduce the efficiency of ichthyoliths observations for the following two reasons. First, particles have to be
120 positioned on the imaged slides without overlap, which can be practically difficult when using glass slides.
121 Second, ichthyoliths are translucent when observed under a polarized light microscope, which makes
122 determining an appropriate threshold challenging.
123 Here, as a first step toward using deep learning for ichthyolith observation, we describe a deep learning based
124 system that can detect microfossil fish teeth from glass slide images and predict their lengths. The system is
125 composed of open-source libraries, so that it can be readily applied to a range of detection problems within the
126 geosciences.

2. Materials and Methods

2.1. System overview

Our system is divided into two parts: (1) the detection of fossil fish teeth from slide images by a single-class object detection model and (2) the precise classification of the detected particles by a two-class classification model (Fig. 1), each described in the following sections.

The system is designed to require little manual work. The initial detection results by Mask R-CNN model are exported to an Excel sheet. Then, in the classification by EfficientNet-V2, images of individual particles are automatically generated from the slide images and the Excel sheet. This means that there is no need to export all the Mask R-CNN detection results to an image (which would take up a lot of data space), or to manually move files from one folder to another.

2.1.1 Detection using Mask R-CNN

The slide images are processed using the object detection model "Mask R-CNN." Mask R-CNN is an open-source model that is capable of semantic segmentation and has a deep-learning-based algorithm that predicts the label in every pixel of an image (He et al., 2017). ResNet-101 (He et al., 2016) was used as the backbone of the model. Training was performed to minimalize loss function originally defined for the Mask R-CNN model, which consists of the sum of losses in classification, predictions of bounding boxes, and masks (He et al., 2017). The stochastic gradient descent with momentum (SGDM) with a momentum of 0.9 was used as an optimizer and the initial learning rate was set to 0.001. The input image size was set to 640 × 640 pixels.

2.1.2 Re-classification using EfficientNet-V2

Although the fully trained Mask R-CNN model can predict the classes of the objects detected, we found that the model was unable to learn the features of fish teeth with our dataset. Therefore, we combined it with another open source deep learning model, 'EfficientNet-V2' (Tan and Le, 2021), which discriminates the classes of the particles detected by the Mask R-CNN model. Images of particles detected by Mask R-CNN were resized to 224 × 224 pixels without changing the aspect ratio. These images are then classified into 'tooth' or 'noise' classes by the trained EfficientNet-V2 model. Training of EfficientNet-V2 model was performed to minimize categorical cross entropy implemented in the Python library keras (Ketkar, 2017). An SGDM with a momentum of 0.9 was used as an optimizer and the initial learning rate was set to 0.005. The class determined by the image-classification model was taken as the final class predicted by the system. In other words, even if a particle was predicted as a "tooth" by the Mask R-CNN model, it was considered "noise" if it was classified as such by the EfficientNet-V2 model.

2.2 Experiments

2.2.1 Preparation of slide images

Glass slides were prepared from the pelagic clay samples collected at Ocean Drilling Program (ODP) Site 1179 and piston core site MR15-E01 PC11 in the western North Pacific Ocean, and Integrated Ocean Drilling Program (IODP) Sites U1366 and U1370 in the South Pacific Ocean. The locations and water depths of these

163 sites are summarized in Table S1. The method for preparing the slides followed previous studies on the
164 determination of depositional ages (Doyle and Riedel, 1985; Ohta et al., 2020) with some modifications as
165 described by Sibert et al. (2017). Approximately 5 g of the wet sediment sample was first well mixed with
166 deionized water in a plastic bottle, and then sieved through a 62 μm mesh to collect the larger particles. Heavy
167 liquid separation was then used to concentrate biogenic calcium phosphate grains. The particles were well mixed
168 with a solution of sodium polytungstate (SPT; specific gravity = 2.80−2.85 g/cm^3) and centrifuged at 1000−1500
169 rpm. The collected particles were washed with deionized water, placed on glass slides using a pipette, dried at
170 40 °C, and then sealed with a cover glass using a light-curing adhesive. Microscopic images of the entire area of
171 the prepared slides were automatically captured using an RX-100 digital microscope (Hirox Co., Ltd.). This
172 microscope has a motorized stage that moves gradually to divide the observation area into small squares, which
173 can be continuously imaged. The magnification of the microscope was 200× (each pixel = 0.96 × 0.96 μm), and
174 approximately 1000 images of 1200 × 1200 pixels were generated from a single slide.
175
176 2.2.2. Training of the object detection model
177 A total of 958 slide images with at least one ichthyolith were prepared to train the Mask R-CNN model. For
178 these images, ichthyolith contour and class information was annotated using the VGG Image Annotator (Dutta
179 and Zisserman, 2019). The dataset was randomly split into a training dataset, which was composed of 958
180 images with annotation data for 1625 teeth, and a validation dataset composed of 92 images and annotation data

for 165 teeth.

The mask R-CNN model training was conducted using the online cloud service Paperspace (https://www.paperspace.com/). To augment the dataset, the images were randomly flipped upside down and/or left-to-right during the training. The initial learning rate was set at 0.001, and the model was trained for 80 epochs. The progress of learning was monitored by calculating the losses implemented in the Mask R-CNN library for both the training and validation datasets.

2.2.3. Training the image classification model

Particles within the slide images were trimmed from the classification model dataset. These particles were manually labeled into the 'tooth' and 'noise' classes. Examples of 'noisy' particles are fish bones, opaque grains that are possibly micro ferromanganese (Fe-Mn) oxides (Yasukawa et al., 2020), and the edges of light-curing adhesives (see Fig. 1b). The EfficientNet-V2 model was trained using the Google Colaboratory Cloud service (Carneiro et al., 2018). During the training, the images were randomly flipped upside down and/or left-to-right to prevent overfitting. The learning rate was set at 0.005, and the model was trained for 20 epochs. The progress of the learning was monitored by calculating the losses and accuracies for both the training and validation datasets.

2.2.4. Tests for the practical use of the system

In addition to the validation of each model, we conducted a practical test to verify the performance of the entire

system. A total of 5177 slide images from six glass slides were generated from a single sample (ODP Site 1179, section 24, Core 5, 75−77 cm interval). This sample was not used for any of the training or validation datasets. Annotation data for the locations of the 431 teeth within the images were prepared. The images were first subjected to detection using the trained Mask R-CNN model. By comparing the annotated data and the model predictions, the number of true positives (TPs), false positives (FPs), and false negatives (FNs) were determined. TPs represent the numbers of teeth that were correctly predicted as teeth by the model. FPs represent the numbers of non-teeth particles that were incorrectly predicted as teeth. FNs represent the numbers of teeth that were not detected by the model. Using these values, several evaluation parameters were calculated as follows:

$$\text{Precision} = \frac{TP}{TP + FP} \quad \ldots (1)$$

$$\text{Recall} = \frac{TP}{TP + FN} \quad \ldots (2)$$

$$\text{F1 score} = \frac{2(Precision \times Recall)}{Precision + Recall} \quad \ldots (3)$$

Precision represents the extent to which the model misclassified particles as teeth. Recall represents the extent to which the model failed to detect teeth. The F1 score is the harmonic mean of precision and recall, indicating the overall balance of the model. After evaluation of the Mask R-CNN model detection results, all of the detected particles were re-classified using the EfficientNet-V2 model, and the precision, recall, and F1 scores were recalculated.

2.3 Measurement of ichthyolith length

The dimensions of ichthyoliths are key for their accurate classification. Here, we defined the length of a tooth as the perpendicular length from the apex of the outline to the lowest level (Fig. 2a) based on the traditional ichthyolith description system (Doyle and Riedel, 1979). Given that variation in tooth length can be used as an indicator of variation in the body sizes of pelagic fish (Britten and Sibert, 2020), we attempted to predict the lengths of teeth automatically, by approximating the detected contours of each tooth within a rectangle and measuring the length of the longest side (Fig. 2b). This approach was based on the assumption that most teeth have an elongated shape (Britten and Sibert, 2020). To evaluate the accuracy of the acquired lengths, tooth lengths were manually measured in the images using the following three steps: (1) the start and end points of measurement were determined manually based on the definition in traditional ichthyolith biostratigraphy, (2) distance between start and end points was measured in pixels using a PC application named "PhotoRuler" (http://inocybe.info/_userdata/ruler/help-eng.html), and (3) the distance in pixels was converted to μm using the resolution of the image (1 pixel corresponds to 0.96 μm).

3. Results and Discussion

3.1 Detection of fish teeth

Figure S1 shows the loss function trend for each training epoch. Although the loss values for the training dataset gradually decreased, the loss for the validation dataset oscillated within the range of 0.5−1.2 and did not show

any significant decrease. This indicates that the model could not sufficiently learn the general features of the teeth. A practical test was performed using the trained model up to epoch 80. Although the model achieved 99.3% recall, the precision was 5.5% (Fig. 3).

The loss function and accuracy trends for the training and validation datasets during each epoch of the EfficientNet-V2 model training are shown in Fig. S2. With regard to the training data, there was a decrease in loss and an increase in accuracy up to epoch 20. The validation data also showed a decrease in loss and an increase in accuracy up to epoch 10, and maintained low losses and high accuracy without oscillation during epochs 10–20. This suggests that the model successfully learned the general features of the teeth without overfitting the training dataset. The model trained up to epoch 19 was selected as the best model, when the lowest validation loss was recorded, and was subjected to the practical test. By combining the Mask R-CNN model trained up to epoch 80 and the EfficientNet-V2 model trained until epoch 19, a practical test was performed as described in Section 2.2.4. By testing 11 thresholding confidence scores from 0.1 to 0.6 at 0.05 increments, we determined the best threshold score to be 0.45, where the highest F1 score was achieved (Table S2). At this threshold score, the practical test resulted in 78.6% of recall, 89.0% of precision and 83.5% of F1 score.

Detection by the Mask R-CNN model alone resulted in high recall and very low precision, which may be due to the loose criteria for judging particles as teeth. Using this model, almost all the ichthyoliths were correctly detected, while many non-tooth particles were incorrectly classified as teeth by the trained Mask R-CNN model.

252 Therefore, Mask R-CNN model alone does not represent a time-saving approach because manual intervention is
253 still needed to correctly identify ichthyoliths from a large number of detected particles.
254 On the contrary, the combined system showed significantly higher precision and slightly lower recall (Fig. 3).
255 This indicates that the EfficientNet-V2 model is effective at identifying fish teeth from the large number of
256 particles detected by the Mask R-CNN model. The F1 score was 83.5%, which is 8 times higher than that of the
257 Mask R-CNN model when used alone.
258 For application of this system in stratigraphic research, it is important to detect clear and distinct ichthyoliths
259 with a small number of false positives, even if small and obscure ichthyoliths are not detected. In this case, a
260 threshold score of 0.45 should be used to obtain the highest F1 score. In environmental research, the total
261 number of ichthyoliths within a sample is an important proxy. A threshold score of 0.1 and manually checking
262 the detection results can minimize the occurrence of false negatives. Although this approach requires some
263 manual labor, it is much more time-efficient than the previous handpicking process..
264

265 ## 3.2 Measurement of ichthyolith length

266 The scatter diagram for the lengths of the teeth predicted by the contours of the detection results and manually
267 measured lengths is shown in Fig. 4. In three cases (out of 341), the predicted lengths were significantly shorter
268 than the measured length, which occurred when the Mask R-CNN model was unable to determine the contours
269 of the model. However, overall, the predicted lengths of 90.6% of the detected teeth were within ± 20% of their

measured lengths. This indicates that as well as their detection and classification, our system provides an efficient means of determining the length distribution of fossil fish teeth.

3.3 Implications for the wider application of object detection in the geosciences

There are many fields within the geosciences in which images are used to detect and/or count target objects (Ohta et al., 2016, 2020; Takahashi et al., 2009; Usui et al., 2017). Automation of these tasks using object detection techniques has the potential to acquire a greater number of results and enable more comprehensive investigation than has been previously possible. However, object detection has not yet been widely applied in the geosciences, with the exception of remote sensing (Zhang et al., 2020). This can be attributed to the difficulty in generating the large learning datasets required for precise detection. This is hindered by the requirement for special equipment, such as microscopes (polarizing microscopy, stereoscopic microscopy, and scanning electron microscopy) and computed tomography (CT) scanners. This has cost, time, and manual labor implications that can make the acquisition of a large number of images impractical. Second, the annotation process of object detection often requires skilled expertise, compared with more applied fields of research such as robotics, medicine, and materials science, and devoting sufficient resources (both budgetary and personnel) to the annotation process may be less prioritized in this field.

Our study shows that a relatively small dataset (< 1000 microscopic images containing approximately 1800 teeth) is sufficient to train the Mask R-CNN model to detect the contours of possible teeth, although when used

alone, it was not sufficient to distinguish the teeth precisely. Therefore, the best overall performance was achieved by fully training a model focused on the classification of the predicted regions, which requires much less time and manual labor than preparing a large dataset for the Mask R-CNN model. This indicates that challenging object detection problems can be efficiently addressed by dividing the task into two subtasks i.e., extracting the contours of candidate objects and then precisely classifying the objects based on the extracted contours. This implies that object detection may be applied in various fields in the geosciences, especially where the acquisition of large training datasets for object detection has proven to be challenging.

4. Conclusions

We developed and tested a system to detect fossil fish teeth from slide images by combining two open source deep learning models—the object detection model 'Mask R-CNN' and the image classification model 'EfficientNet-V2'. The system provided results with 89.0% precision, 78.6% recall, and an F1 score of 83.5% in a test that assumed realistic conditions, indicating its potential for practical application. In addition, the system successfully derived the lengths of 90% of the detected teeth with an accuracy of ± 20%. As such, the system has potential for constraining both the depositional ages and environments of deep-sea sediments and, more broadly, contributing to research on the evolution of the marine ecosystem. Additional work is now being undertaken to update the EfficientNet-V2 model so that ichthyoliths can be further classified into morphological taxa. This requires a larger dataset of ichthyolith images, which could be compiled with the support of the system

306 constructed in this study.

307 Competing interests

308 The authors declare that they have no competing interests.

309

310 Funding

311 This research was funded by the Japan Society for the Promotion of Science (JSPS) KAKENHI grant numbers

312 20H05658 to YK, 17H01361 to KN, 19J14560 and 21K20354 to KM.

313

314 Acknowledgements

315 The authors thank T. Itaki at the National Institute of Advanced Industrial Science and Technology for a

316 preliminary discussion on the separation of ichthyoliths and the use of deep learning for microfossil observations.

317 We would also like to thank A. Takeuchi, M. Shimbo, Y. Yoshikawa, and Y. Shigeto at Chiba Institute of

318 Technology for their advice on developing deep learning models.

319 Data Availability

320 Datasets related to this article can be found at http://dx.doi.org/10.17632/zdpz6m9gzf.1, an open-source online

321 data repository hosted at Mendeley Data (Mimura, 2022).

322

323 Code Availability

324 The sample codes for application of Mask R-CNN and EfficientNet-V2 for microfossils detection proble

ms are on GitHub (https://github.com/KazuhideMimura/ai_ichthyolith; https://github.com/KazuhideMimura/eNetV2_for_ai_ichthyolith).

References

Apostol, L.A., Márquez, E., Gasmen, P., Solano, G., 2016. RadSS: A radiolarian classifier using support vector machines, in: 7th International Conference on Information, Intelligence, Systems & Applications (IISA) 2016. IEEE Publications, pp. 1–6.

Beaufort, L. Dollfus, D., 2004. Automatic recognition of coccoliths by dynamical neural networks, Marine Micropaleontology 51, 57–73.

Bi, D., Shi, X., Huang, M., Yu, M., Zhou, T., Zhang, Y., Zhu, A., Shi, M., Fang, X., 2021. Geochemical and mineralogical characteristics of deep-sea sediments from the western North Pacific Ocean: Constraints on the enrichment processes of rare earth elements. Ore Geology Reviews 138, 104318.

Bi, H., Guo, Z., Benfield, M.C., Fan, C., Ford, M., Shahrestani, S., Sieracki, J.M., 2015. A semi-automated image analysis procedure for in situ plankton imaging systems. PLOS ONE 10, e0127121.

Britten, G.L., Sibert, E.C., 2020. Enhanced fish production during a period of extreme global warmth. Nature Communications 11, 5636.

Carneiro, T., Medeiros Da Nobrega, R.V., Nepomuceno, T., Bian, G., De Albuquerque, V.H.C., Filho, P.P.R., 2018. Performance analysis of google colaboratory as a tool for accelerating deep learning applications. IEEE Access 6, 61677–61685.

Carvalho, L.E., Fauth, G., Baecker Fauth, S.B., Krahl, G., Moreira, A.C., Fernandes, C.P., Von Wangenheim, A., 2020. Automated microfossil identification and segmentation using a deep learning approach. Marine Micropaleontology 158, 101890.

Doyle, P.S., Kennedy, G.G., Riedel, W.R., 1974. Stratigraphy, in: Davies, T.A., Luyendyk, B.P., et al. (Eds.), Initial Reports of the Deep Sea Drilling Project 26, Washington (U.S. Government Printing Office), pp. 825–905.

Doyle, P.S., Riedel, W.R., 1979. Ichthyoliths: Present status of taxonomy and stratigraphy of microscopic fish skeletal debris. Scripps Institution Of Oceanography Reference Series. 79–16. Publications. National Technical Information Service, Springfield, Virginia, 22161, 1–231.

Doyle, P.S., Riedel, W.R., 1985. Cenozoic and Late Cretaceous ichthyoliths, in: Bolli, H.M., Saunders, J.B., Perch-Nielsen, K. (Eds.), Plankton Stratigraphy. Cambridge University Press, pp. 965–995.

Dunlea, A.G., Murray, R.W., Sauvage, J., Pockalny, R.A., Spivack, A.J., Harris, R.N., D'Hondt, S., 2015b. Cobalt-based age models of pelagic clay in the South Pacific Gyre. Geochemistry, Geophysics, Geosystems 16, 2694–2710.

Dunlea, A.G., Murray, R.W., Sauvage, J., Spivack, A.J., Harris, R.N., D'Hondt, S., 2015a. Dust, volcanic ash, and the evolution of the South Pacific Gyre through the Cenozoic. Paleoceanography 30, 1078–1099.

Dutkiewicz, A., Müller, R.D., O'Callaghan, S., Jónasson, H., 2015. Census of seafloor sediments in the world's ocean. Geology 43, 795–798.

Dutta, A., Zisserman, A., 2019. The via annotation software for images, audio and video, in: Proceedings of the 27th ACM International Conference on Multimedia, pp. 2276–2279.

Fujinaga, K., Yasukawa, K., Nakamura, K., Machida, S., Takaya, Y., Ohta, J., Araki, S., Liu, H., Usami, R., Maki, R., Haraguchi, S., Nishio, Y., Usui, Y., Nozaki, T., Yamazaki, T., Ichiyama, Y., Ijiri, A., Inagaki, F., Machiyama, H., Iijima, K., Suzuki, K., Kato, Y., KR13-02, MR13-E02 Leg 2, KR14-02 Cruise members., 2016. Geochemistry of REY-rich mud in the Japanese Exclusive Economic Zone around Minamitorishima Island. Geochemical Journal 50, 575–590 Leg. 2.

He, K., Zhang, X., Ren, S., Sun, J., 2016. Deep residual learning for image recognition. In Proceedings of the IEEE Conference on Computer Vision and Pattern Recognition, pp. 770–778.

He, K., Gkioxari, G., Dollar, P., Girshick, R., 2017. Mask R-CNN. IEEE Transactions on Pattern Analysis and Machine Intelligence 42, 386–397.

Hsiang, A.Y., Brombacher, A., Rillo, M.C., Mleneck-Vautravers, M.J., Conn, S., Lordsmith, S., Jentzen, A., Henehan, M.J., Metcalfe, B., Fenton, I.S., Wade, B.S., Fox, L., Meilland, J., Davis, C.V., Baranowski, U., Groeneveld, J., Edgar, K.M., Movellan, A., Aze, T., Dowsett, H.J., Miller, C.G., Rios, N., Hull, P.M., 2019. Endless Forams: > 34,000 modern planktonic foraminiferal images for taxonomic training and automated species recognition using convolutional neural networks. Paleoceanography and Paleoclimatology 34, 1157–1177.

Hsiang, A.Y., Nelson, K., Elder, L.E., Sibert, E.C., Kahanamoku, S.S., Burke, J.E., Kelly, A., Liu, Y., Hull, P.M.,

2018. AutoMorph: Accelerating morphometrics with automated 2D and 3D image processing and shape extraction. Methods in Ecology and Evolution 9, 605–612.

Hu, Q., Davis, C., 2005. Automatic plankton image recognition with co-occurrence matrices and support vector machine. Marine Ecology Progress Series 295, 21–31.

Iijima, K., Yasukawa, K., Fujinaga, K., Nakamura, K., Machida, S., Takaya, Y., Ohta, J., Haraguchi, S., Nishio, Y., Usui, Y., Nozaki, T., Yamazaki, T., Ichiyama, Y., Ijiri, A., Inagaki, F., Machiyama, H., Suzuki, K., Kato, Y., KR13-02 Cruise members, 2016. Discovery of extremely REY-rich mud in the western North Pacific Ocean. Geochemical Journal 50, 557–573.

Itaki, T., Taira, Y., Kuwamori, N., Maebayashi, T., Takeshima, S., Toya, K., 2020. Automated collection of single species of microfossils using a deep learning–micromanipulator system. Progress in Earth and Planetary Science 7, 1–7.

Jo, Y., Park, S., Jung, J., Yoon, J., Joo, H., Kim, M.H., Kang, S.J., Choi, M.C., Lee, S.Y., Park, Y., 2017. Holographic deep learning for rapid optical screening of anthrax spores. Science Advances 3, e1700606.

Kato, Y., Fujinaga, K., Nakamura, K., Takaya, Y., Kitamura, K., Ohta, J., Toda, R., Nakashima, T., Iwamori, H., 2011. Deep-sea mud in the Pacific Ocean as a potential resource for rare-earth elements. Nature Geoscience 4, 535–539.

Ketkar, N. 2017. Introduction to Keras. In: Deep Learning with Python. Apress, Berkeley, CA. https://doi.org/10.1007/978-1-4842-2766-4_7

Keçeli, A.S., Kaya, A., Keçeli, S.U., 2017. Classification of radiolarian images with hand-crafted and deep features. Computers & Geosciences 109, 67–74.

Kim, J., Cho, H., Hwangbo, M., Choi, J., Canny, J., Kwon, Y.P., 2018. Deep traffic light detection for self-driving cars from a large-scale dataset, in: 21st International Conference on Intelligent Transportation Systems (ITSC) 2018. IEEE Publications, pp. 280–285.

Kyte, F.T., 1998. A meteorite from the Cretaceous/Tertiary boundary. Nature. 396, 237–239.

Kyte, F.T., Bostwick, J.A., 1995. Magnesioferrite spinel in Cretaceous/Tertiary boundary sediments of the Pacific basin: Remnants of hot, early ejecta from the Chicxulub impact? Earth and Planetary Science Letters 132, 113–127.

Kyte, F.T., Leinen, M., Ross Heath, G.R., Zhou, L., 1993. Cenozoic sedimentation history of the central North Pacific: Inferences from the elemental geochemistry of core LL44-GPC3. Geochimica et Cosmochimica Acta 57, 1719–1740.

Leinen, M., 1987. The origin of paleochemical signatures in North Pacific pelagic clays: Partitioning experiments. Geochimica et Cosmochimica Acta 51, 305–319.

Marchant, R., Tetard, M., Pratiwi, A., Adebayo, M., de Garidel-Thoron, T., 2020. Automated analysis of foraminifera fossil records by image classification using a convolutional neural network. Journal of Micropalaeontology 39, 183–202.

Marmo, R., Amodio, S., Cantoni, V., 2006. Microfossils shape classification using a set of width values, in: 18th

International Conference on Pattern Recognition (ICPR'06) 1. IEEE Publications.

Menendez, A., James, R.H., Roberts, S., Peel, K., Connelly, D., 2017. Controls on the distribution of rare earth elements in deep-sea sediments in the North Atlantic Ocean. Ore Geology Reviews 87, 100–113.

[dataset] Mimura, K., 2022. Datasets for ichthyolith detection, Mendeley Data, V1, doi: 10.17632/zdpz6m9gzf.1

Mimura, K., Nakamura, K., Yasukawa, K., Machida, S., Ohta, J., Fujinaga, K., Kato, Y., 2019. Significant impacts of pelagic clay on average chemical composition of subducting sediments: New insights from discovery of extremely rare-earth elements and yttrium-rich mud at Ocean Drilling Program Site 1149 in the western North Pacific Ocean. Journal of Asian Earth Sciences 186, 104059.

Mitra, R., Marchitto, T.M., Ge, Q., Zhong, B., Kanakiya, B., Cook, M.S., Fehrenbacher, J.S., Ortiz, J.D., Tripati, A., Lobaton, E., 2019. Automated species-level identification of planktic foraminifera using convolutional neural networks, with comparison to human performance. Marine Micropaleontology 147, 16–24.

Müller, R.D., Cannon, J., Qin, X., Watson, R.J., Gurnis, M., Williams, S., Pfaffelmoser, T., Seton, M., Russell, S.H.J., Zahirovic, S., 2018. GPlates: Building a virtual Earth through deep time. Geochemistry, Geophysics, Geosystems 19, 2243–2261.

Nakamura, K., Fujinaga, K., Yasukawa, K., Takaya, Y., Ohta, J., Machida, S., Haraguchi, S., Kato, Y., 2015. REY-rich mud: A deep-sea mineral resource for rare earths and yttrium, in: Handbook on the Physics and Chemistry of Rare Earths, Elsevier 46, pp. 79–127.

Nozaki, T., Ohta, J., Noguchi, T., Sato, H., Ishikawa, A., Takaya, Y., Kimura, J.I., Chang, Q., Shimada, K., Ishibashi, J.I., Yasukawa, K., Kimoto, K., Iijima, K., Kato, Y., 2019. A Miocene impact ejecta layer in the

pelagic Pacific Ocean. Scientific Reports 9, 16111.

Ohta, J., Yasukawa, K., Machida, S., Fujinaga, K., Nakamura, K., Takaya, Y., Iijima, K., Suzuki, K., Kato, Y., 2016. Geological factors responsible for REY-rich mud in the western North Pacific Ocean: Implications from mineralogy and grain size distributions. Geochemical Journal 50, 591–603.

Ohta, J., Yasukawa, K., Nakamura, K., Fujinaga, K., Iijima, K., Kato, Y., 2021. Geological features and resource potential of deep-sea mud highly enriched in rare-earth elements in the Central Pacific Basin and the Penrhyn Basin. Ore Geology Reviews 139, 104440.

Ohta, J., Yasukawa, K., Nozaki, T., Takaya, Y., Mimura, K., Fujinaga, K., Nakamura, K., Usui, Y., Kimura, J.I., Chang, Q., Kato, Y., 2020. Fish proliferation and rare-earth deposition by topographically induced upwelling at the Late Eocene cooling event. Scientific Reports 10, 9896.

Pires de Lima, R., Welch, K.F., Barrick, J.E., Marfurt, K.J., Burkhalter, R., Cassel, M., Soreghan, G.S., 2020. Convolutional neural networks as an aid to biostratigraphy and micropaleontology: A test on Late Paleozoic microfossils. Palaios 35, 391–402.

Ren, J., Liu, Y., Wang, F., He, G., Deng, X., Wei, Z., Yao, H., 2021. Mechanism and influencing factors of REY enrichment in deep-sea sediments. Minerals 11, 196.

Sa, R., Sun, X., He, G., Xu, L., Pan, Q., Liao, J., Zhu, K.C., Deng, X., 2018. Enrichment of rare earth elements in siliceous sediments under slow deposition: A case study of the central North Pacific. Ore Geology Reviews 94, 12–23.

Sakai, Y., Takemoto, S., Hori, K., Nishimura, M., Ikematsu, H., Yano, T., Yokota, H., 2018. Automatic detection of early gastric cancer in endoscopic images using a transferring convolutional neural network, In: 40th Annual International Conference of the IEEE Engineering in Medicine and Biology Society (EMBC). IEEE Publications. 2018, 4138–4141.

Shoji, D., Noguchi, R., Otsuki, S., Hino, H., 2018. Classification of volcanic ash particles using a convolutional neural network and probability. Scientific Reports 8, 8111.

Sibert, E., Friedman, M., Hull, P., Hunt, G., Norris, R., 2018. Two pulses of morphological diversification in Pacific pelagic fishes following the Cretaceous–Palaeogene mass extinction. Proceedings. Biological sciences 285.

Sibert, E., Norris, R., Cuevas, J., Graves, L., 2016. Eighty-five million years of Pacific Ocean gyre ecosystem structure: Long-term stability marked by punctuated change. Proceedings. Biological sciences 283.

Sibert, E.C., Cramer, K.L., Hastings, P.A., Norris, R.D., 2017. Methods for isolation and quantification of microfossil fish teeth and elasmobranch dermal denticles (ichthyoliths) from marine sediments. Palaeontologia Electronica 20, 1–14.

Sibert, E.C., Hull, P.M., Norris, R.D., 2014. Resilience of Pacific pelagic fish across the Cretaceous/Palaeogene mass extinction. Nature Geoscience 7, 667–670.

Sibert, E.C., Rubin, L.D., 2021. An Early Miocene extinction in pelagic sharks. Science 372, 1105–1107.

Sibert, E.C., Zill, M.E., Frigyik, E.T., Norris, R.D., 2020. No state change in pelagic fish production and

biodiversity during the Eocene–Oligocene transition. Nature Geoscience 13, 238–242.

Solano, G.A., Gasmen, P., Marquez, E.J., 2018. Radiolarian classification decision support using supervised and unsupervised learning approaches, in: 9th International Conference on Information, Intelligence, Systems and Applications (IISA) 2018. IEEE Publications, pp. 1–6.

Suleymanova, I., Balassa, T., Tripathi, S., Molnar, C., Saarma, M., Sidorova, Y., Horvath, P., 2018. A deep convolutional neural network approach for astrocyte detection. Scientific Reports 8, 12878.

Takahashi, S., Yamakita, S., Suzuki, N., Kaiho, K., Ehiro, M., 2009. High organic carbon content and a decrease in radiolarians at the end of the Permian in a newly discovered continuous pelagic section: A coincidence? Palaeogeography, Palaeoclimatology, Palaeoecology 271, 1–12.

Takaya, Y., Yasukawa, K., Kawasaki, T., Fujinaga, K., Ohta, J., Usui, Y., Nakamura, K., Kimura, J.I., Chang, Q., Hamada, M., Dodbiba, G., Nozaki, T., Iijima, K., Morisawa, T., Kuwahara, T., Ishida, Y., Ichimura, T., Kitazume, M., Fujita, T., Kato, Y., 2018. The tremendous potential of deep-sea mud as a source of rare-earth elements. Scientific Reports 8, 5763.

Tan, M., Le, Q., 2021. Efficientnetv2: Smaller models and faster training, in: International Conference on Machine Learning, pp. 10096–10106. PMLR.

Tanaka, E., Nakamura, K., Yasukawa, K., Mimura, K., Fujinaga, K., Iijima, K., Nozaki, T., Kato, Y., 2020a. Chemostratigraphy of deep-sea sediments in the western North Pacific Ocean: Implications for genesis of mud highly enriched in rare-earth elements and yttrium. Ore Geology Reviews 119, 103392.

Tanaka, E., Nakamura, K., Yasukawa, K., Mimura, K., Fujinaga, K., Ohta, J., Iijima, K., Nozaki, T., Machida, S., Kato, Y., 2020b. Chemostratigraphic correlations of deep-sea sediments in the western North Pacific Ocean: A new constraint on the distribution of mud highly enriched in rare-earth elements. Minerals 10, 575.

Tanaka, E., Yasukawa, K., Nakamura, K., Ohta, J., Miyazaki, T., Vaglarov, B.S., Machida, S., Fujinaga, K., Iwamori, H., Kato, Y., 2022. Secular variations in provenance of sedimentary components in the western North Pacific Ocean constrained by Sr isotopic features of deep-sea sediments. Geochemistry, Geophysics, Geosystems, e2021GC009729.

Tetard, M., Marchant, R., Cortese, G., Gally, Y., de Garidel-Thoron, T., Beaufort, L., 2020. Technical note: A new automated radiolarian image acquisition, stacking, processing, segmentation and identification workflow. Climate of the Past. 16, 2415–2429.

Usui, Y., Yamazaki, T., Saitoh, M., 2017. Changing abundance of magnetofossil morphologies in pelagic red clay around Minamitorishima, western North Pacific. Geochemistry, Geophysics, Geosystems 18, 4558–4572.

Westerhold, T., Marwan, N., Drury, A.J., Liebrand, D., Agnini, C., Anagnostou, E., Barnet, J.S.K., Bohaty, S.M., De Vleeschouwer, D., Florindo, F., Frederichs, T., Hodell, D.A., Holbourn, A.E., Kroon, D., Lauretano, V., Littler, K., Lourens, L.J., Lyle, M., Pälike, H., Röhl, U., Tian, J., Wilkens, R.H., Wilson, P.A., Zachos, J.C., 2020. An astronomically dated record of Earth's climate and its predictability over the last 66 million years.

Science 369, 1383–1387.

Xu, Y., Dai, Z., Wang, J., Li, Y., Wang, H., 2020. Automatic recognition of palaeobios images under microscope based on machine learning. IEEE Access 8, 172972–172981.

Yasukawa, K., Kino, S., Azami, K., Tanaka, E., Mimura, K., Ohta, J., Fujinaga, K., Nakamura, K., Kato, Y., 2020. Geochemical features of Fe-Mn micronodules in deep-sea sediments of the western North Pacific Ocean: Potential for co-product metal extraction from REY-rich mud. Ore Geology Reviews 127, 103805.

Yasukawa, K., Liu, H., Fujinaga, K., Machida, S., Haraguchi, S., Ishii, T., Nakamura, K., Kato, Y., 2014. Geochemistry and mineralogy of REY-rich mud in the eastern Indian Ocean. Journal of Asian Earth Science 93, 25–36.

Yasukawa, K., Nakamura, K., Fujinaga, K., Iwamori, H., Kato, Y., 2016. Tracking the spatiotemporal variations of statistically independent components involving enrichment of rare-earth elements in deep-sea sediments. Scientific Reports 6, 29603.

Yasukawa, K., Nakamura, K., Fujinaga, K., Machida, S., Ohta, J., Takaya, Y., Kato, Y., 2015. Rare-earth, major, and trace element geochemistry of deep-sea sediments in the Indian Ocean: Implications for the potential distribution of REY-rich mud in the Indian Ocean. Geochemical Journal 49, 621–635.

Yasukawa, K., Ohta, J., Mimura, K., Tanaka, E., Takaya, Y., Usui, Y., Fujinaga, K., Machida, S., Nozaki, T., Iijima, K., Nakamura, K., Kato, Y., 2018. A new and prospective resource for scandium: Evidence from the geochemistry of deep-sea sediment in the western North Pacific Ocean. Ore Geology Reviews 102,

524 260–267.

525 Yasukawa, K., Ohta, J., Miyazaki, T., Vaglarov, B.S., Chang, Q., Ueki, K., Toyama, C., Kimura, J.I., Tanaka, E.,
526 Nakamura, K., Fujinaga, K., Iijima, K., Iwamori, H., Kato, Y., 2019. Statistic and isotopic characterization
527 of deep-sea sediments in the western North Pacific Ocean: Implications for genesis of the sediment
528 extremely enriched in rare earth elements. Geochemistry, Geophysics, Geosystems 20, 3402–3430.

529 Yu, M., Shi, X., Huang, M., Liu, J., Yan, Q., Yang, G., Li, C., Yang, B., Zhou, T., Bi, D., Wang, H., Bai, Y.,
530 2021. The transfer of rare earth elements during early diagenesis in REY-rich sediments: An example from
531 the Central Indian Ocean Basin. Ore Geology Reviews 136, 104269.

532 Yu, S., Saint-Marc, P., Thonnat, M., Berthod, M., 1996. Feasibility study of automatic identification of planktic
533 foraminifera by computer vision. The Journal of Foraminiferal Research 26, 113–123.

534 Zachos, J.C., Dickens, G.R., Zeebe, R.E., 2008. An Early Cenozoic perspective on greenhouse warming and
535 carbon-cycle dynamics. Nature 451, 279–283.

536 Zhang, X., Han, L., Han, L., Zhu, L., 2020. How well do deep learning-based methods for land cover
537 classification and object detection perform on high resolution remote sensing imagery? Remote Sensing 12,
538 417.

539 Zhang, X., Tao, C., Shi, X., Li, H., Huang, M., Huang, D., 2017. Geochemical characteristics of REY-rich
540 pelagic sediments from the GC02 in central Indian Ocean Basin. Journal of Rare Earths 35, 1047–1058.

541 Zhou, L., Kyte, F.T., 1992. Sedimentation history of the South Pacific pelagic clay province over the last 85

542 million years inferred from the geochemistry of Deep Sea Drilling Project Hole 596. Paleoceanography 7,
543 441–465.
544 Zhou, T., Shi, X., Huang, M., Yu, M., Bi, D., Ren, X., Liu, J., Zhu, A., Fang, X., Shi, M., 2021. Genesis of
545 REY-rich deep-sea sediments in the Tiki Basin, eastern South Pacific Ocean: Evidence from geochemistry,
546 mineralogy and isotope systematics. Ore Geology Reviews 138, 104330.
547 Zhou, T., Shi, X., Huang, M., Yu, M., Bi, D., Ren, X., Yang, G., Zhu, A., 2020. The influence of hydrothermal
548 fluids on the REY-rich deep-sea sediments in the Yupanqui Basin, eastern South Pacific Ocean:
549 Constraints from bulk sediment geochemistry and mineralogical characteristics. Minerals 10, 1141.
550 Ziegler, C.L., Murray, R.W., Hovan, S.A., Rea, D.K., 2007. Resolving eolian, volcanogenic, and authigenic
551 components in pelagic sediment from the Pacific Ocean. Earth and Planetary Science Letters 254, 416–
552 432.
553

554 ## List of Figures

559

2. Figure 2: (a) Examples of “measured lengths” based on traditional ichthyolith biostratigraphy, and (b) photographs showing the method to obtain “predicted length” estimation methods.

3. Figure 3: Precisions, recalls, and F1 scores from the practical test. The bars on the left side indicate the results when the regions of fish teeth were predicted by the Mask R-CNN alone, while the bars on the right represent the results predicted by the combined system of Mask R-CNN and EfficientNet-V2.

4. Figure 4: Comparison of mechanically predicted and manually measured ichthyolith lengths. Dashed line in red is an identical line ($y = x$), and that in blue is a regression line ($y = 0.93x - 3.71$). The three crossed points are outliers that were not used for calculation of regression lines. The yellow band indicates that predicted length is within ±20% of the measured length.

5. Figure S1: Losses for training and validation datasets during the training of the Mask R-CNN model. Blue line indicates the loss calculated for training dataset and the orange one indicates the loss for validation dataset.

6. Figure S2: (a) Losses and (b) accuracies for training and validation datasets during the training of the EfficientNet-V2 model. Blue and orange lines indicate the values calculated for training and validation

datasets, respectively.

List of Tables

(a) detection

object detection model “Mask R-CNN”

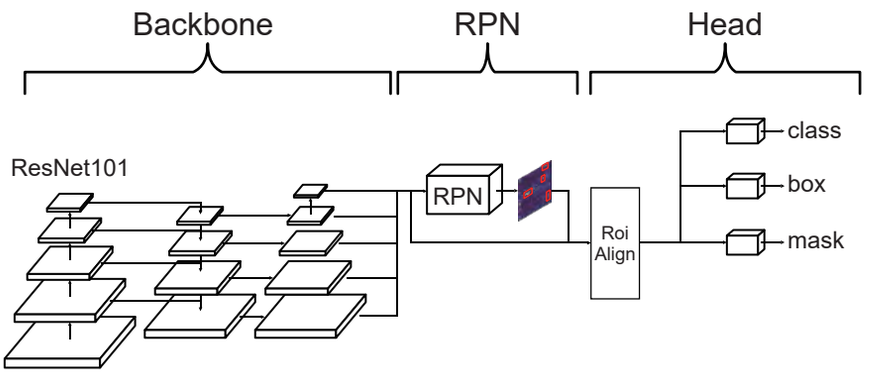

inputs:
slide images

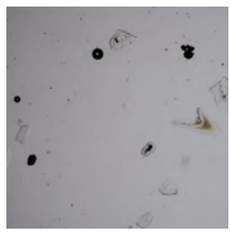

outputs:
locations of possible teeth

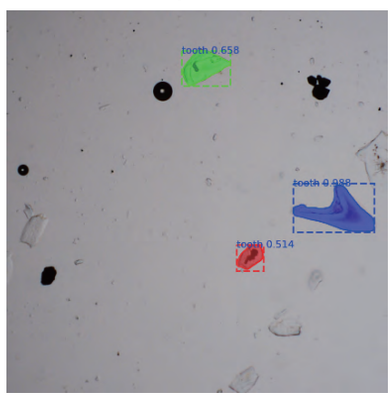

(b) classification

inputs: particles detected by Mask R-CNN

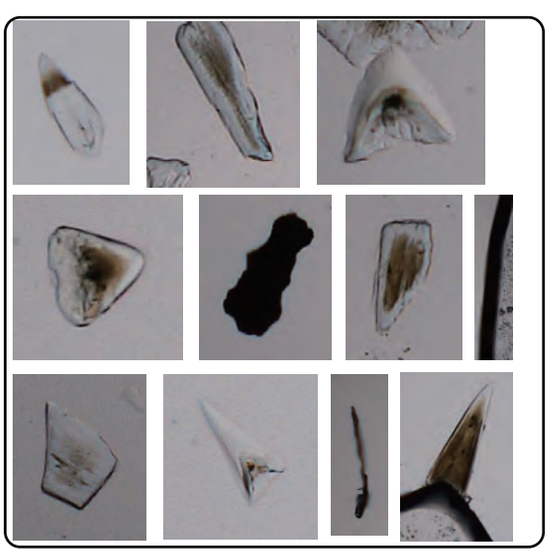

classification model
EfficientNet-V2

outputs: classes of the images

class ‘tooth’

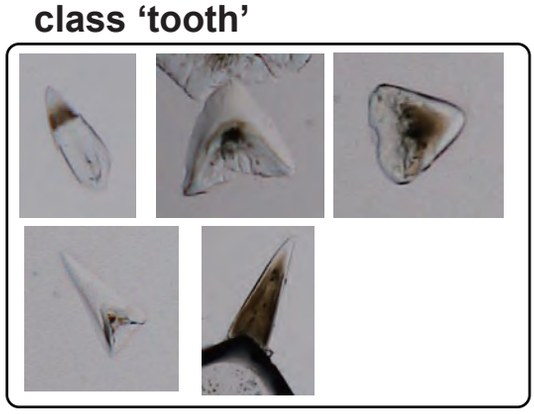

class ‘noise’

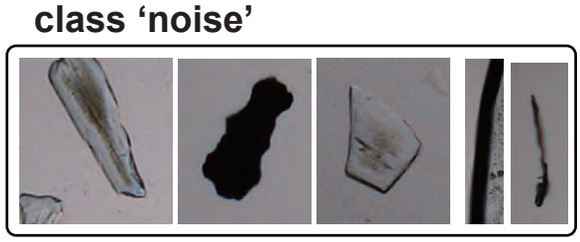

Figure 1

(a) Manually measured length

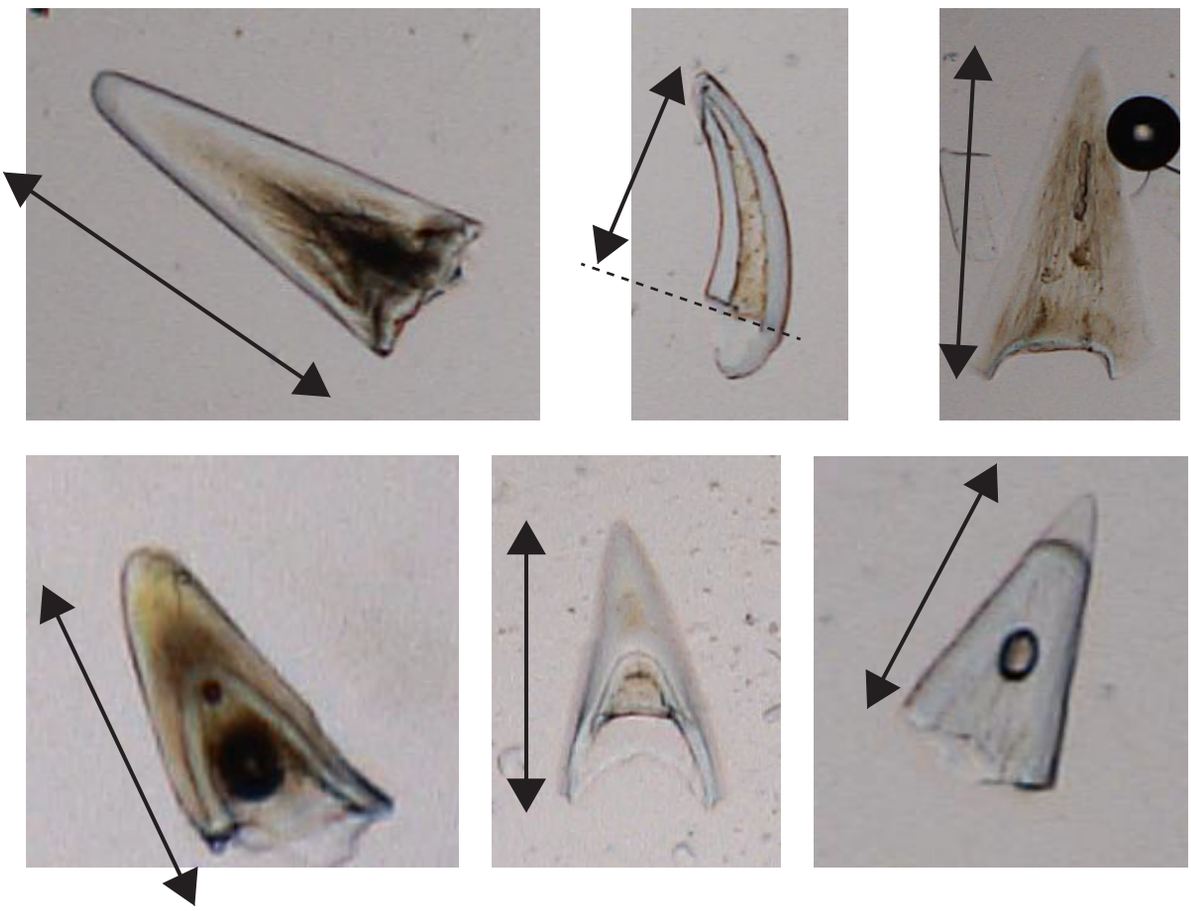

(b) Prediction of length by contour

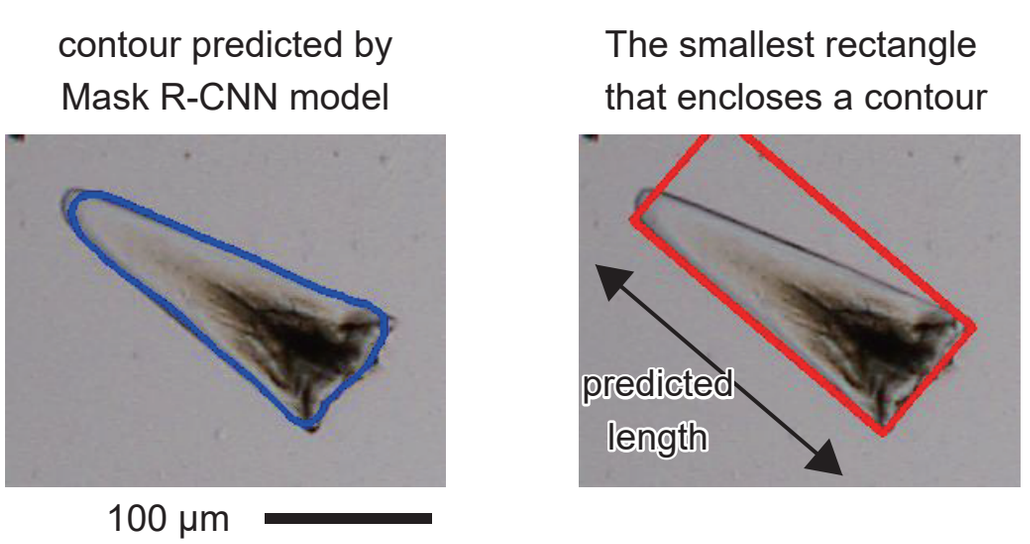

Figure 2

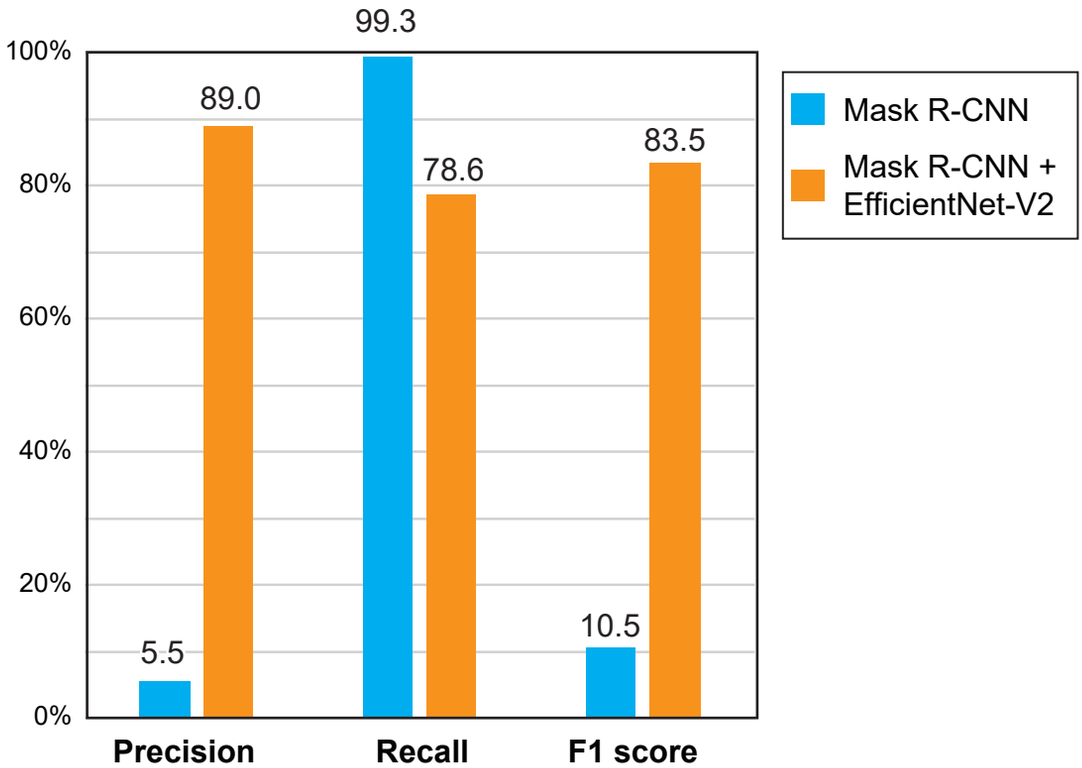
99.3
100%
89.0
83.5
80%
78.6
60%
40%
20%
10.5
5.5
0%
Precision
Recall
F1 score
Mask R-CNN
Mask R-CNN +
EfficientNet-V2

Figure 3

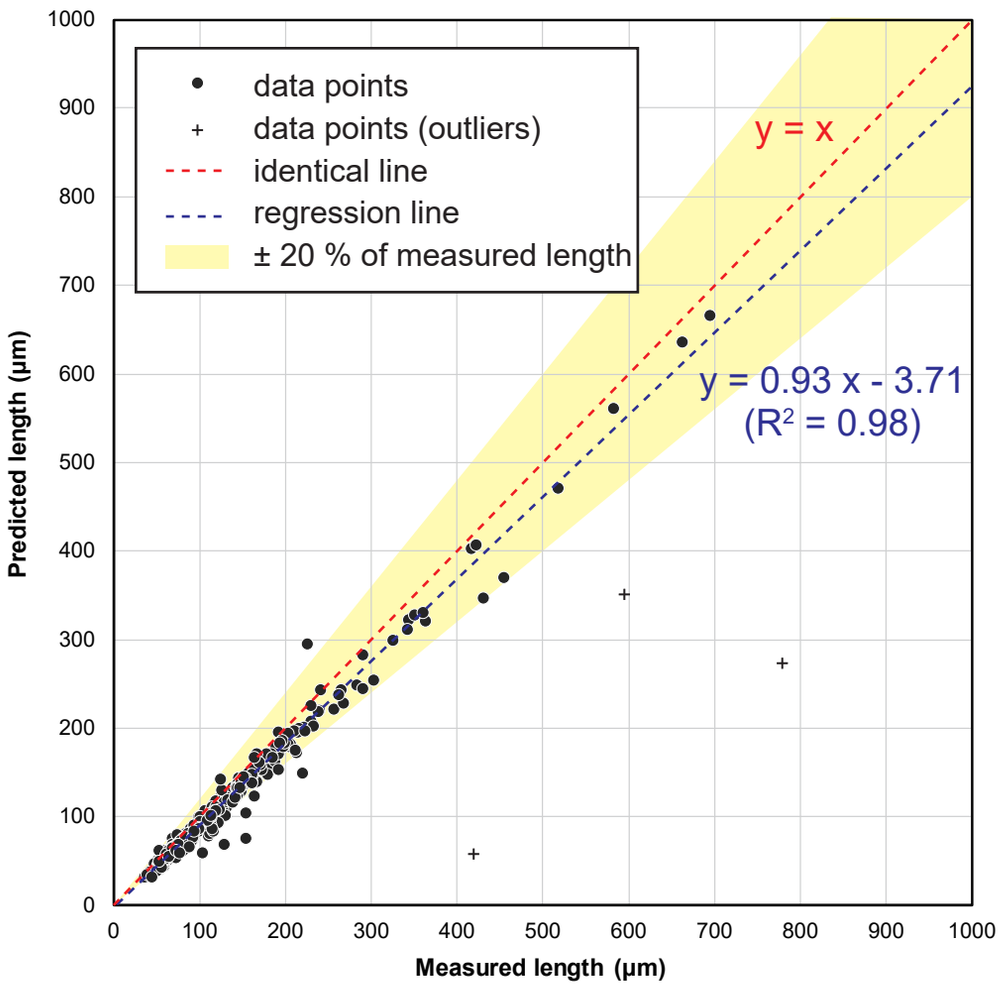
data points
data points (outliers)
identical line
regression line
± 20 % of measured length
y = x
y = 0.93 x - 3.71
(R² = 0.98)
Predicted length (µm)
Measured length (µm)
0
100
200
300
400
500
600
700
800
900
1000

Figure 4

Supplementary Information for:

Automated detection of microfossil fish teeth from slide images using combined deep learning models

Kazuhide Mimura, Shugo Minabe, Kentaro Nakamura, Kazutaka Yasukawa, Junichiro Ohta, Yasuhiro Kato

Supplementary information includes:

Supplementary Tables S1, S2

Supplementary Figures S1, S2

Table S1. Locations and water depths of the analyzed sites.

ODP/DSDP	Leg/Cruise	Site	Hole	Latitude	Longitude	Water depth [m]
ODP	191	1179	C	41°04.7871' N	159°57.7856' E	5,563.9
IODP	Exp. 329	U1366	C	26°03.0845' S	156°53.6700' W	5,129.5
		U1370	D	41°51.1156' S	153°06.3812' W	5,073.0
-	MR15-E01	PC11	-	21°58.2732’ N	153°47.7461’ W	5,770

Table S2. Results of the practical test with varying threshold confidence scores of the EfficientNet-V2 model.

threshold score	Recall	Precision	F1 value
0.1	90.8	61.9	73.6
0.15	86.4	74.1	79.8
0.2	84.8	79.0	81.8
0.25	83.2	81.1	82.1
0.3	80.9	82.8	81.8
0.35	80.2	85.1	82.6
0.4	79.0	87.3	83.0
0.45	**78.6**	**89.0**	**83.5**
0.5	77.6	89.9	83.3
0.55	77.4	90.3	83.4
0.6	76.3	91.4	83.2

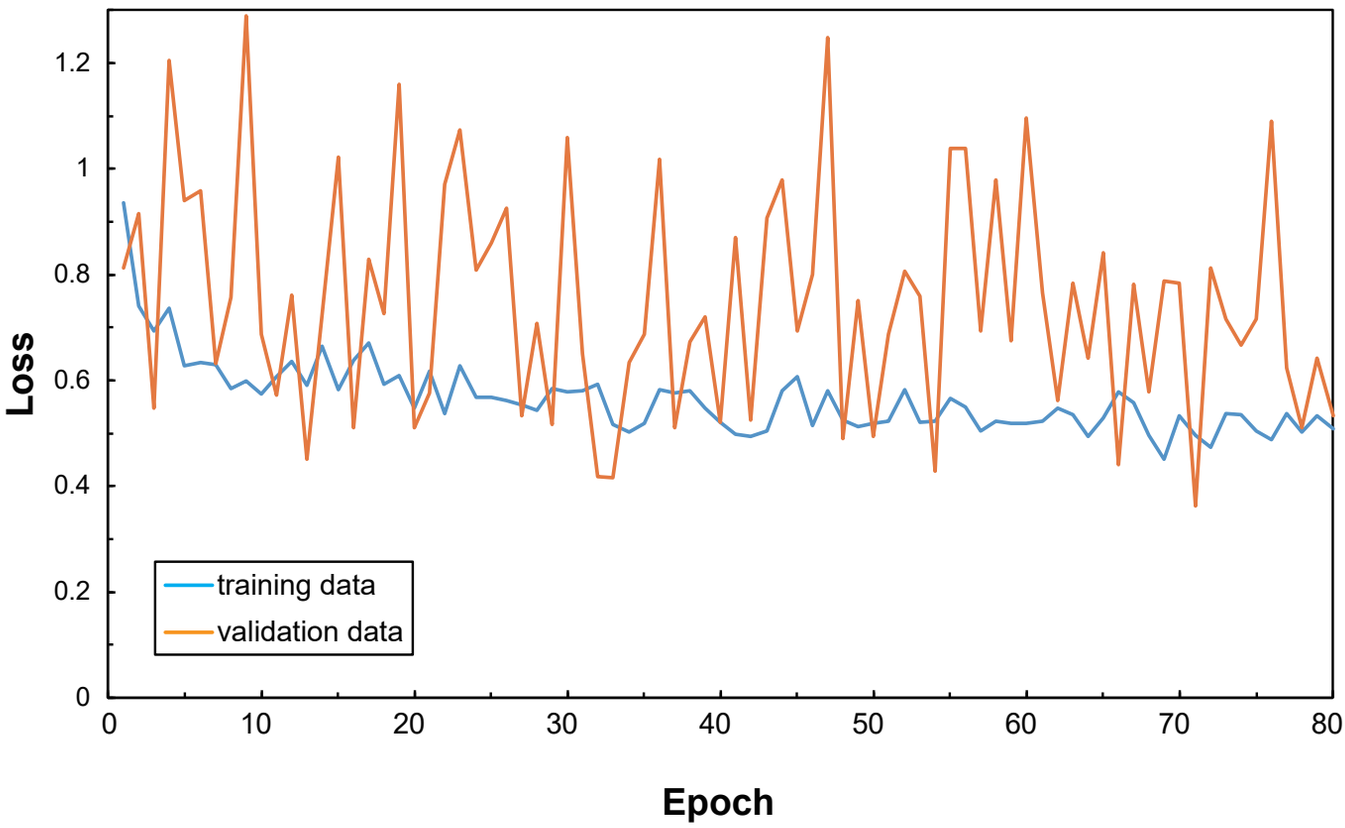

Fig. S1. Losses for training and validation datasets during the training of the Mask R-CNN model. Blue line indicates the loss calculated for training dataset and orange one indicates the loss for validation dataset.

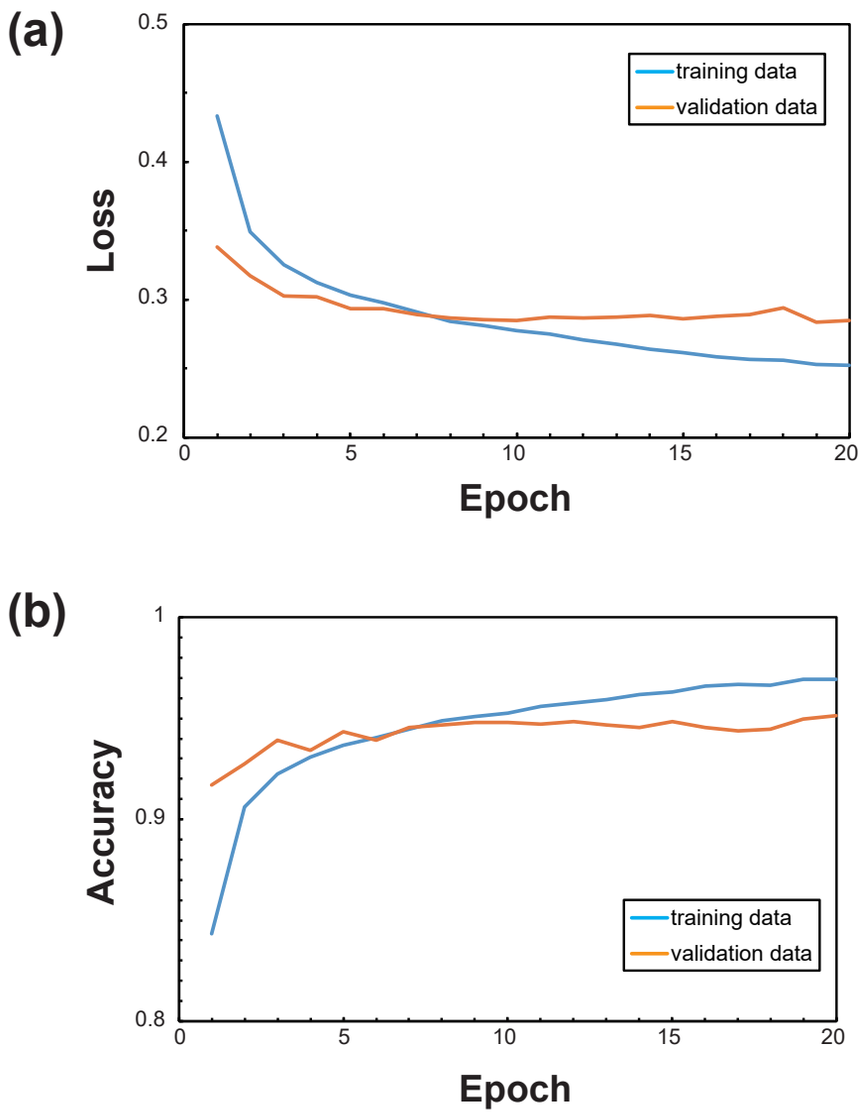

Fig. S2. (a) Losses and (b) accuracies for training and validation datasets during the training of the EfficientNet-V2 model. Blue and orange lines indicate the values calculated for training and validation datasets, respectively.